



Unlocking anionic redox activity in O3-type sodium 3d layered oxides via Li substitution

Qing Wang^{1,2,3}, Sathiya Mariyappan^{1,4}, Gwenaëlle Rouse^{1,2,4}, Anatolii V. Morozov⁵, Benjamin Porcheron^{4,6}, Rémi Dedryvère^{4,7}, Jinpeng Wu⁸, Wanli Yang⁸, Leiting Zhang⁹, Mohamed Chakir³, Maxim Avdeev^{10,11}, Michaël Deschamps^{4,6}, Young-Sang Yu⁸, Jordi Cabana¹², Marie-Liesse Doublet^{4,13}, Artem M. Abakumov⁵ and Jean-Marie Tarascon^{1,2,4} ✉

Sodium ion batteries, because of their sustainability attributes, could be an attractive alternative to Li-ion technology for specific applications. However, it remains challenging to design high energy density and moisture stable Na-based positive electrodes. Here, we report an O3-type NaLi_{1/3}Mn_{2/3}O₂ phase showing anionic redox activity, obtained through a ceramic process by carefully adjusting synthesis conditions and stoichiometry. This phase shows a sustained reversible capacity of 190 mAh g⁻¹ that is rooted in cumulative oxygen and manganese redox processes as deduced by combined spectroscopy techniques. Unlike many other anionic redox layered oxides so far reported, O3-NaLi_{1/3}Mn_{2/3}O₂ electrodes do not show discernible voltage fade on cycling. This finding, rationalized by density functional theory, sheds light on the role of inter- versus intralayer 3d cationic migration in ruling voltage fade in anionic redox electrodes. Another practical asset of this material stems from its moisture stability, hence facilitating its handling and electrode processing. Overall, this work offers future directions towards designing highly performing sodium electrodes for advanced Na-ion batteries.

Rechargeable lithium ion batteries have empowered the success of consumer devices, and are continuing to conquer the market of electric vehicles¹. However, there still remains a rising demand for more sustainable and cost-effective cathode materials for large-scale energy storage. The Na-ion technology, because of the Na abundance as compared to Li, offers an alternative solution to fill this gap, provided improvements are made in terms of energy density^{2,3}. Towards this goal, inspired by the discovery of high capacity in Li-rich layered oxides relying on cumulative cationic and anionic redox processes^{4–6}, great efforts have been devoted to the design of Na-rich layered oxides (Na(Na_xM_{1–y})O₂, $y < 1$; M, transition metal cation(s)). Commonly, anionic redox in layered oxides is triggered by the introduction of alkali metals into the MO₂^{6–} layer that generates oxygen lone pairs associated with oxygen non-bonding 2p states in the electronic structure^{7,8}. Implementing this strategy to Na-layered oxides is not simple due to the size mismatch between NaO₆ and MO₆ octahedra.

To contour such a difficulty, researchers have prepared Na-rich layered oxides with large and highly covalent 4d and/or 5d metals (Ru, Ir and so on)^{9–13}. In contrast, in the presence of 3d metals, anionic redox is solely reported with non-stoichiometric P2/P3-type Na_xA_yM_{1–y}O₂ ($0 < x < 1$, $y < 1$) phases, where the non-bonding O 2p orbitals are made available by increasing the O/M ratio compared to NaMO₂ using Li⁺/Mg²⁺/Zn²⁺/vacancies as the A cation instead of Na⁺ (refs. 14–20). However, practical-wise P2/P3 phases fall short in achieving the high energy density target because of their Na deficiency²¹. Hence, the standing challenge resides in the synthesis

of anionic redox active sodium layered oxides consisting of 3d transition metals while having full sodium stoichiometry (O3-type Na(A,M)O₂ with Na/(A,M) of 1). Such complexity of having proper alkali content has even been predicted by density functional theory (DFT) and confirmed experimentally, since the authors of ref. 22 synthesized P2-Na_{0.75}Li_{0.25}Mn_{0.75}O₂ instead of the desired NaLi_{1/3}Mn_{2/3}O₂. Using the expertise from our early study on stabilizing the NaLi_{1/3}Ir_{2/3}O₂ phase²³, we herein explore the Na–Li composition balance in the NaLi_xMn_{1–y}O₂ series to stabilize an anionic redox active O3 structure with full Na content and successfully synthesize a new NaLi_{1/3}Mn_{2/3}O₂ phase.

A survey of various key parameters (Li/Mn ratio, nature of precursors, annealing temperature, flushing gases) was conducted and the results are summarized in Supplementary Figs. 1–3 with the optimized synthesis conditions explained in the Methods. The single-phase material was solely obtained for the composition NaLi_{1/3}Mn_{2/3}O₂ by heating a ball-milled mixture of Na₂O₂, Li₂O and Mn₂O₃ at 700 °C in a tubular furnace that was flushed with argon before calcination. The X-ray powder diffraction (XRD) pattern of the as-synthesized material corresponds to an O3-type structure with minute amounts of an impurity phase that was washed away by soaking the sample in distilled water (Supplementary Figs. 1 and 4). The resulting sample was stable on exposure to moist air (Supplementary Fig. 5), had a composition of Na_{0.97}Li_{0.32}Mn_{0.68}O₂ deduced from inductively coupled plasma–optical emission spectrometry (ICP–OES) analysis and is hereafter referred to as NaLi_{1/3}Mn_{2/3}O₂ for the purposes of simplicity.

¹Chimie du Solide-Energie, UMR 8260, Collège de France, Paris, France. ²Sorbonne Université, Paris, France. ³Renault, Technocentre, Guyancourt, France.

⁴Réseau sur le Stockage Electrochimique de l'Energie (RS2E), Amiens, France. ⁵Skoltech Center for Energy Science and Technology, Skolkovo Institute of Science and Technology, Moscow, Russia. ⁶CNRS, CEMHTI UPR3079, Université d'Orléans, Orléans, France. ⁷IPREM, E2S-UPPA, CNRS,

Univ. Pau & Pays Adour, Pau, France. ⁸Advanced Light Source, Lawrence Berkeley National Laboratory, Berkeley, CA, USA. ⁹Electrochemistry Laboratory, Paul Scherrer Institute, Villigen, Switzerland. ¹⁰School of Chemistry, The University of Sydney, Sydney, New South Wales, Australia. ¹¹Australian Centre for Neutron Scattering, Australian Nuclear Science and Technology Organisation, Kirrawee DC, New South Wales, Australia. ¹²Department of Chemistry, University of Illinois at Chicago, Chicago, IL, USA. ¹³ICGM, University of Montpellier, CNRS, ENSCM, Montpellier, France.

✉e-mail: jean-marie.tarascon@college-de-france.fr

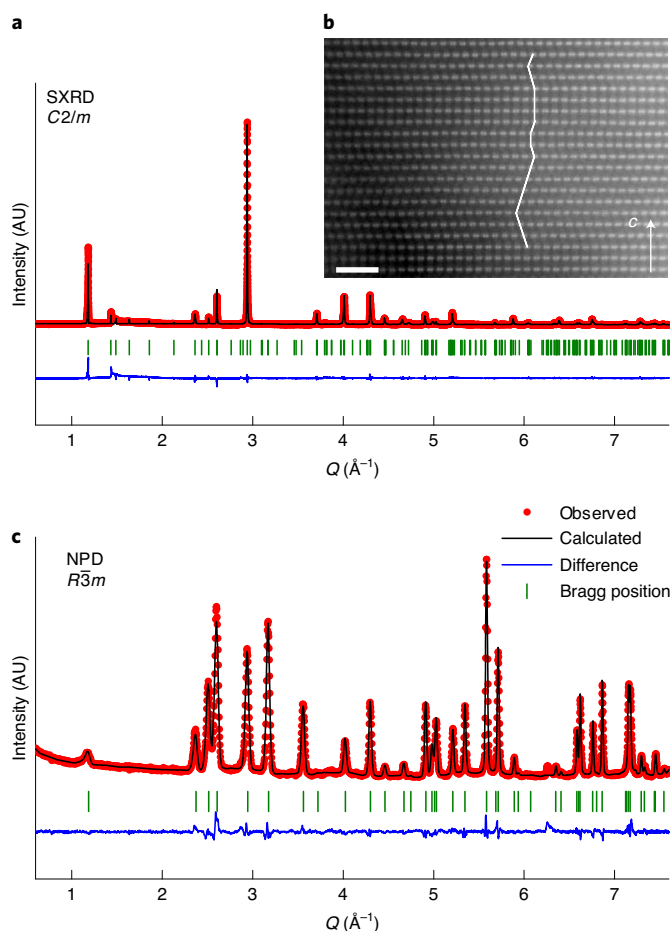


Fig. 1 | Structure of the water-washed pristine material. **a**, Rietveld refinement of the SXR D pattern in $C2/m$ space group ($O3$ -type) of $\text{NaLi}_{1/3}\text{Mn}_{2/3}\text{O}_2$ after being washed in H_2O . Note that such a description indexes the superstructure reflections between 5 and $10^\circ 2\theta$ (Supplementary Fig. 6) arising from $[\text{Li}_{1/3}\text{Mn}_{2/3}]\text{O}_2$ honeycomb ordering. AU, arbitrary units. **b**, $[\bar{1}10]$ HAADF-STEM image of H_2O -washed $\text{NaLi}_{1/3}\text{Mn}_{2/3}\text{O}_2$ (indexes refer to the $R\bar{3}m$ cell). The periodicity along the stacking direction of the ‘honeycomb’ $[\text{Li}_{1/3}\text{Mn}_{2/3}]\text{O}_2$ layers is frequently violated by stacking faults appearing as lateral shifts of the layers (traced with the white line). Scale bar, 2 nm. **c**, Rietveld refinement of the NPD pattern of an H_2O -washed $\text{NaLi}_{1/3}\text{Mn}_{2/3}\text{O}_2$ sample. The $R\bar{3}m$ space group was chosen instead of $C2/m$ to fit the neutron pattern due to the bare visibility of superstructure peaks from the $[\text{Li}_{1/3}\text{Mn}_{2/3}]\text{O}_2$ honeycomb ordering. As the coherent neutron scattering lengths for Mn and Li differ only by a factor of 2 ($b(\text{Mn}) = -0.37$ fm versus $b(\text{Li}) = -0.19$ fm) as compared to a factor of eight for XRD ($Z(\text{Mn}) = 25$ versus $Z(\text{Li}) = 3$), superstructure peaks associated with the honeycomb ordering are less visible in the NPD pattern than in XRD, and even more attenuated in the presence of stacking faults.

Figure 1a shows the synchrotron XRD (SXR D) pattern of the water-washed material. It can be Rietveld refined using two models commonly used to describe an $O3$ structure: either in the $R\bar{3}m$ space group with the lattice parameters $a = 2.92441(1)$ Å, $c = 15.96473(9)$ Å (Supplementary Fig. 6 and Supplementary Table 1), or in the $C2/m$ space group with $a = 5.05911(5)$ Å, $b = 8.77505(6)$ Å, $c = 5.58491(5)$ Å and $\beta = 107.6217(5)^\circ$ (Fig. 1a and Supplementary Table 2). Moreover, the compound presents copious stacking faults as deduced from simulated XRD patterns (Supplementary Fig. 7), with these faults propagating along the c axis^{9,11}, as evidenced by $[\bar{1}10]$ high-resolution high angle annular

dark field-scanning transmission electron microscopy (HAADF-STEM) image (Fig. 1b) and corresponding selected area electron diffraction (SAED) pattern (Supplementary Fig. 7). Neutron powder diffraction (NPD, Fig. 1c and Supplementary Table 3), SXR D and STEM support the structure model where Na takes up octahedral sites in between the $[\text{Li}_{1/3}\text{Mn}_{2/3}]\text{O}_2$ slabs while Li and Mn form a ‘honeycomb’ ordering within the $[\text{Li}_{1/3}\text{Mn}_{2/3}]\text{O}_2$ slabs.

The electrochemical properties of $\text{NaLi}_{1/3}\text{Mn}_{2/3}\text{O}_2$ were examined versus metallic Na within the voltage range of 1.5–4.5 V at the rate of C/8 in Swagelok-type cells (Fig. 2). On oxidation, the voltage rapidly reached a plateau at around 3.6 V followed by a sloping region to reach the ‘ $\text{Na}_{0.09}\text{Li}_{1/3}\text{Mn}_{2/3}\text{O}_2$ ’ composition at 4.5 V. The subsequent discharge profile evolved into an almost S-shaped curve, which persisted on repeated cycles, indicating an electrochemically driven structural transformation during the first charge. Out of 0.9 Na^+ removed during the first charge, only 0.67 Na^+ was reinserted on the following discharge leading to a sustained reversible capacity of roughly 190 mAh g^{-1} on cycling (Fig. 2a). This occurred without any loss of Li as deduced from ICP-OES measurements performed on the fully charged and discharged samples (Supplementary Fig. 8).

A pressure test and online electrochemical mass spectrometry (OEMS) were carried out (Fig. 2b and Supplementary Fig. 9) through the electrochemical charging process. Both techniques confirmed gas release in the first charge, which was predominantly O_2 with the onset at roughly 0.58 Na^+ removal (around 3.8 V versus Na^+/Na^0) as shown by the OEMS data. The cumulated O_2 release through the first cycle (Fig. 2b) amounts to $757 \mu\text{mol g}^{-1}$ yielding the material composition $\text{Na}_{0.09}\text{Li}_{1/3}\text{Mn}_{2/3}\text{O}_{1.86}$ at the end of the charge, whereas almost no O_2 release (less than 1%) was observed in the second charge. Aside from O_2 , note equally the release of CO_2 throughout the cycle (Fig. 2b) that is most probably linked with the decomposition of residual carbonates²⁴ on the material surface and/or from the oxidative decomposition of the electrolyte²⁵. Its occurrence through the second cycle, which at first is surprising, is inherent to our experimental protocol (see the note in Supplementary Fig. 9).

Altogether, the cycling profile and the O_2 gas release in the first cycle are reminiscent of Li-rich layered oxides. However, a striking difference emerges with the neat superposition of the discharge curves on cycling indicating the absence of noticeable voltage fade in $\text{NaLi}_{1/3}\text{Mn}_{2/3}\text{O}_2$ that we further confirmed by plotting the average discharge voltage for the first 40 cycles that remained constant (Fig. 2c, inset). Such a feature is not mirrored in charge, which shows a gradual evolution in the shape of the charge curve on repeated cycling (Supplementary Fig. 10).

To interrogate this asymmetric behaviour (the hysteresis between charge and discharge), we monitored the variation of the equilibrium potential process by the galvanostatic intermittent titration technique (GITT). The GITT voltage profile for the second cycle (Fig. 2d) showed a reminiscent voltage gap (also observed on cycling at a C/50 rate, Supplementary Fig. 11) of 300–500 mV between open-circuit voltages (OCVs) at charge versus discharge, despite very long rest periods of 20 h, which indicates a hysteresis of a thermodynamic nature. We next progressively opened the charge window with each cycle by increasing the upper cut-off voltage (Supplementary Fig. 12). The charge profiles are identical but discharge profiles drop gradually on reaching the high voltage redox process (>3.3 V) with simultaneous rapid growth of the overpotential, therefore indicating that the hysteresis is triggered towards the last 50% of charge, hence defining two domains. They are confirmed by the magnification of the voltage relaxation profiles for weakly and highly charged states (insets Fig. 2d) that show two different equilibrium times.

An operando XRD $\text{NaLi}_{1/3}\text{Mn}_{2/3}\text{O}_2/\text{Na}$ half cell was assembled to structurally probe these two domains (Supplementary Fig. 13).

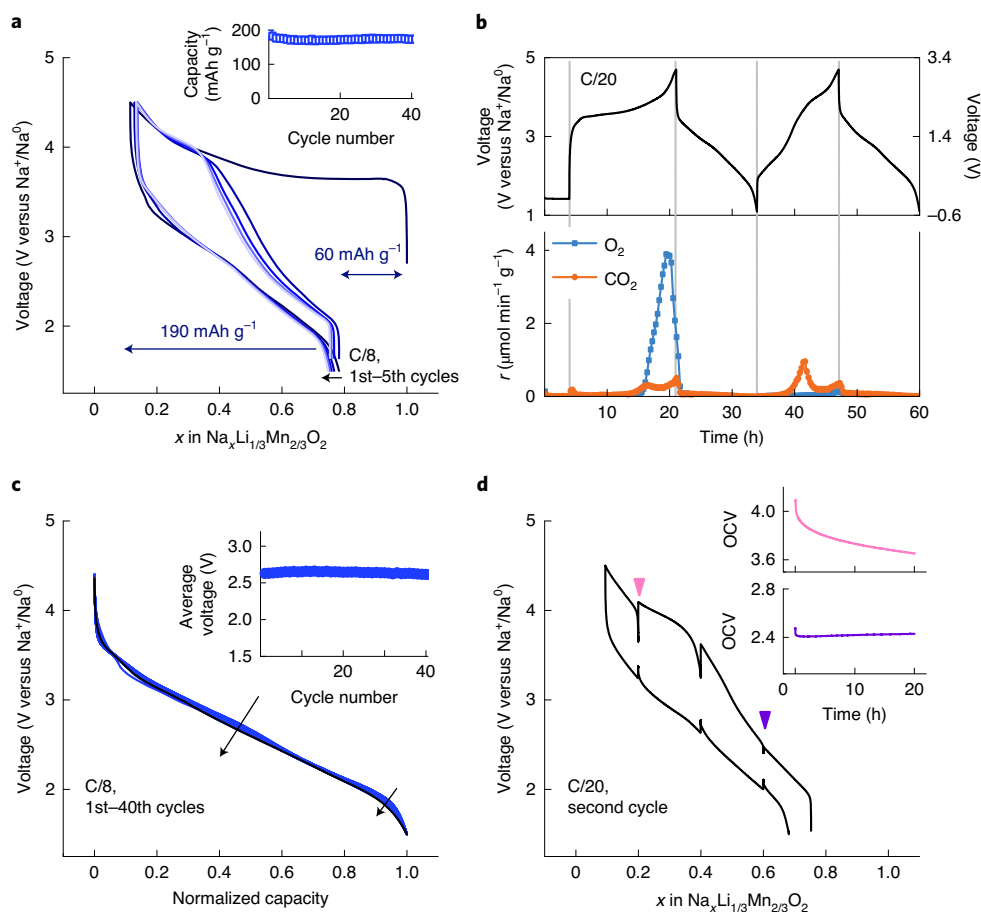


Fig. 2 | Electrochemical behaviour of $\text{NaLi}_{1/3}\text{Mn}_{2/3}\text{O}_2$. **a**, Voltage profile of first five galvanostatic cycles of $\text{NaLi}_{1/3}\text{Mn}_{2/3}\text{O}_2$ against metallic sodium at a C/8 rate ($1C = 285 \text{ mAh g}^{-1}$) between 1.5 and 4.5 V. Inset shows the capacity retention over 40 cycles. **b**, OEMS gas analysis during the first and second cycles of $\text{NaLi}_{1/3}\text{Mn}_{2/3}\text{O}_2$ cycled versus $\text{Na}_3\text{V}_2(\text{PO}_4)_3$ between -0.5 and 3.1 V (right axis), converted to 1.2 – 4.7 V versus Na^+/Na^0 (left axis). The upper panel shows the cycling profile with the observed gas evolution (O_2 ($m/z = 32$) and CO_2 ($m/z = 44$)) in the lower panel. The amount of O_2 released in the first cycle is equal to $757 \mu\text{mol g}^{-1}$ (equivalent to 80 mAh g^{-1} charge capacity). **c**, Normalized discharge curves of the $\text{NaLi}_{1/3}\text{Mn}_{2/3}\text{O}_2/\text{Na}$ half-cell data shown in Fig. 2a for 40 cycles. The inset shows the average discharge voltage calculated without correcting for ohmic drop on cycling. **d**, GITT measurements conducted on the second cycle at a current rate of C/20, with a 20-h relaxation period for every 4 h (0.2 Na^+ exchange). The insets show OCV evolution during 20 h of relaxation at weakly and highly charged states.

Initially, a biphasic process was observed with the appearance of a new phase O3(II) with an increased c lattice parameter compared to the pristine O3(I) phase. Further pursuing the desodiation led to a narrow solid solution through which the c lattice parameter initially contracted before decreasing rapidly, once the O_2 evolution potential was reached, leading to the O3(III) phase at the very end of the charge. For high-quality fitting, ex situ SXR patterns were collected for the intermediate phases that were all indexed in $R\bar{3}m$ (O3 type) since honeycomb superstructure reflections were barely visible (Fig. 3 and Supplementary Tables 4 and 5), as confirmed with electron diffraction (Supplementary Fig. 14). Such a disappearance of superstructure peaks can be either associated with the collapse of the honeycomb ordering due to metal ion migration, or with an increased amount of stacking faults that reduce the long-range ordering.

Further analysing the fully charged oxygen deficient $\text{Na}_{0.09}\text{Li}_{1/3}\text{Mn}_{2/3}\text{O}_2$ phase (O3(III)) as deduced by OEMS, two models with and without oxygen vacancies were tried, but both refinements were of comparable quality preventing reliable assignment (Supplementary Fig. 15). In contrast, models with Mn placed in either octahedral or tetrahedral sites in the Na interlayer space

deteriorate the refinement with respect to the one with Mn solely located in the transition metal layers (Supplementary Fig. 16), suggesting the absence of manganese migration to the alkali layer. This was confirmed by refining the NPD pattern collected for the fully charged sample of which the best fit was obtained with Mn in the metal layers together with all the Li and remaining Na atoms being in the alkali layers, so the resulting chemical formula can be written as $[\text{Na}_{0.09}\text{Li}_{1/3}]_{\text{interlayer}}[(\square_{\text{cat}})_{1/3}\text{Mn}_{2/3}]_{\text{metal}}\text{O}_{1.86}$ where \square_{cat} represents the cation vacancy (Supplementary Fig. 17 and Supplementary Table 6).

HAADF-STEM confirmed the O3-type layered structure of pristine $\text{NaLi}_{1/3}\text{Mn}_{2/3}\text{O}_2$, which was also preserved in the samples charged to 4.5 V and discharged to 1.5 V (Fig. 3d–f). The [010] HAADF-STEM images demonstrate the O3-type stacking by the lateral displacement of the metal layers over one-third of the distance between two neighbouring dots denoting the Mn columns. No additional HAADF intensity was observed between the metal layers (except the very faint dots of the Na columns that are barely visible at the thicker part of the pristine $\text{NaLi}_{1/3}\text{Mn}_{2/3}\text{O}_2$ crystallite (Fig. 3d)), which agrees well with the absence of Mn migration to the Na sites in the charged 4.5 V and discharged to 1.5 V states. The O3 structure was preserved after charge and discharge for ten

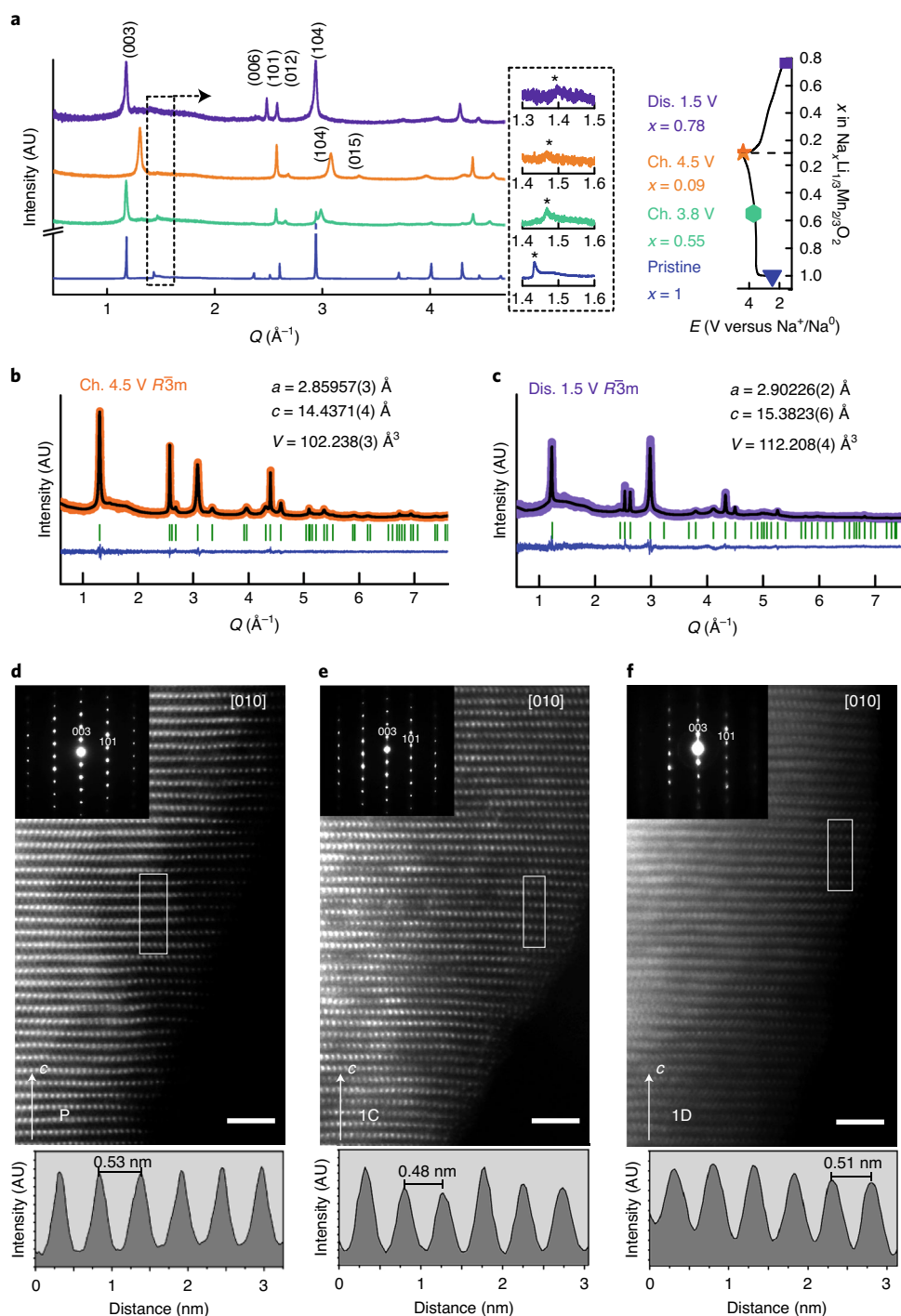


Fig. 3 | Structural evolution in the first cycle. **a**, Left shows SXR patterns of pristine (blue), ex situ samples stopped at mid-charge (green), end of charge (orange) and end of discharge (purple) of the initial cycle. On the right, a zoomed-in view of superstructure peaks (marked by asterisks) together with the ex situ points on the electrochemistry curve. **b,c**, Rietveld refinement of the SXR patterns of the fully charged (**b**) and fully discharged samples (**c**), respectively. All the SXR were indexed in the $R\bar{3}m$ space group ($O3$ structure) and the lattice parameters are mentioned in the figures. **d-f**, Structural analysis by microscopy. $[010]$ HAADF-STEM images and corresponding HAADF intensity profiles across the metal layers in the outlined rectangular areas for pristine (P) (**d**), charged to 4.5 V (1C) (**e**) and discharged to 1.5 V (1D) (**f**) samples. Corresponding $[010]$ SAED patterns are given in the insets; the patterns are indexed as the $O3$ $R\bar{3}m$ phase. The peaks in the HAADF intensity profiles correspond to the Mn columns solely at the metal layers, whereas absence of the intensity between the peaks indicates no Mn migration into the Na layers. Scale bars, 2 nm.

cycles (Supplementary Fig. 18), the reflections in the SAED patterns were very broad and streaked with diffuse intensity along the c^* axis, in line with the enormous anisotropic broadening observed

from SXR (Supplementary Fig. 19). HAADF-STEM images show pronounced local structure distortions, where the metal layers demonstrate strong local variations of the interlayer distance. Mn

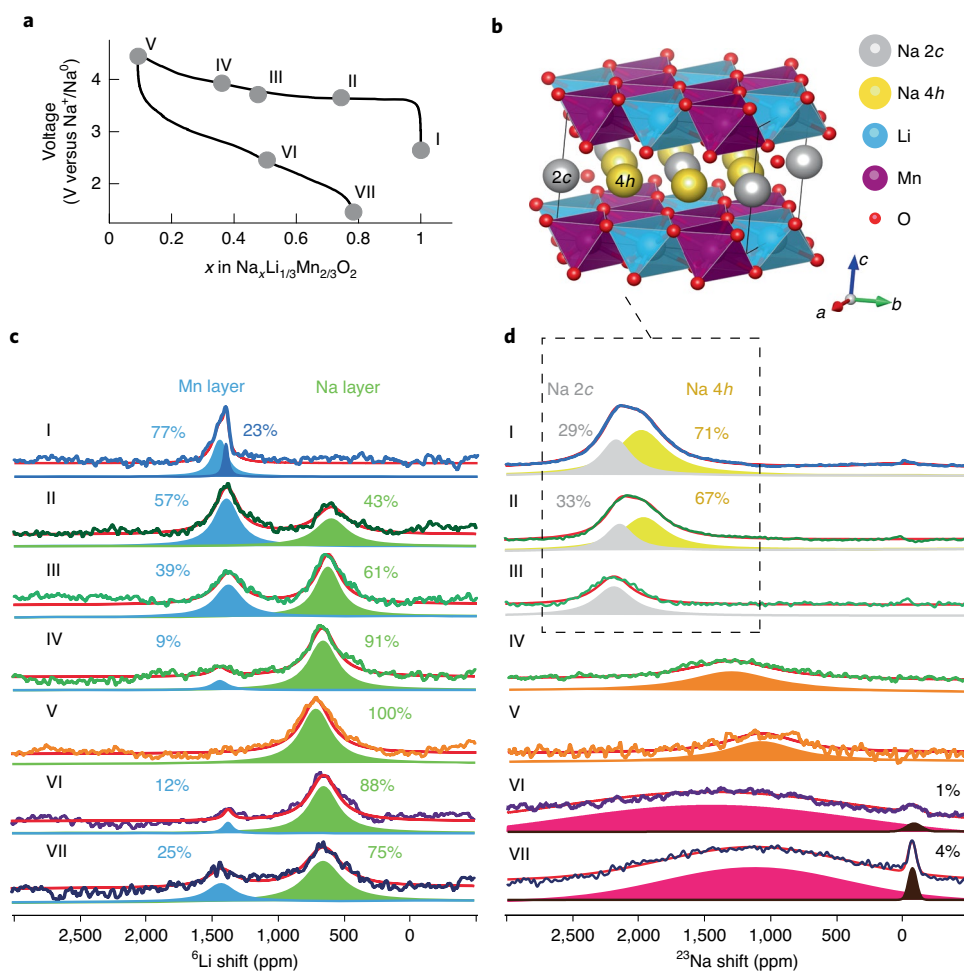


Fig. 4 | ⁶Li and ²³Na MAS NMR spectroscopy results. **a**, First cycle charge–discharge voltage profile with points indicating states of charge or discharge at which the ex situ samples were extracted. **b**, Crystal structure of the pristine NaLi_{1/3}Mn_{2/3}O₂ (space group C2/m) showing two Wyckoff sites (2c and 4h) for Na⁺. **c**, ⁶Li MAS NMR spectra showing two types of peak corresponding to the isotropic shifts for Li in the metal layers (blue) and alkali layers (green). **d**, ²³Na MAS NMR results showing peak shifts and broadening. The two Na⁺ signals in the pristine material can be understood by the two distinct crystal sites shown in **b**. The two sharp peaks at nearly 0 ppm in VI and VII are due to trace amounts of remaining Na salt from the electrolyte that was left unwashed.

migration to the interlayer space occurs only at the surface areas, and not in the bulk parts. Another feature is the substantial suppression of the honeycomb ordering visible in both the SAED pattern and HAADF–STEM image (Supplementary Fig. 18). Overall, combined SXR and TEM results confirm the absence of out-of-plane Mn migration in Na_xLi_{1/3}Mn_{2/3}O₂ with signs, however, of in-plane migration increasing with cycling.

In absence of Li⁺ loss from the structure, as deduced from ICP–OES, we investigated the role of Li during the Na (de)insertion process using ⁶Li and ²³Na nuclear magnetic resonance (NMR) spectra of Na_xLi_{1/3}Mn_{2/3}O₂ (Fig. 4). Both ⁶Li (Fig. 4c) and ²³Na (Fig. 4d) spectra show two signals for the pristine material with different ratios. The doublet for Na stems from the two different Na environments (2c and 4h) for Na⁺ in the C2/m structure (Fig. 4b). The shift to around 1,400 ppm in the ⁶Li Lorentzian line confirms the presence of lithium in the transition metal [Li_{1/3}Mn_{2/3}]O₂ layer²⁶. The splitting into two lines at 1,400 and 1,450 ppm most probably arises from the difference in Li position due to the frequent violation of periodicity along the stacking direction of the honeycomb metal layers (Fig. 1b and Supplementary Fig. 7). On charging, this signal (blue) progressively disappears to the expense of a new one (green) centred

around 700 ppm that is assigned to Li⁺ ions sitting in octahedral coordination within the alkali metal layers^{27,28}, in full agreement with the NPD data (Supplementary Fig. 17 and Supplementary Table 6). This Li-migration is partly irreversible since the peak at 700 ppm remains large (75% of the total) at full discharge (Fig. 4c) and is probably responsible for the wavy nature of the metal layers and the strong local variations of the interlayer distances observed by HAADF–STEM.

Turning to the ²³Na NMR spectra, on charging, this first shows the progressive disappearance of the 1,980 ppm shift (yellow) to the benefit of the 2,170 ppm one (grey) indicating the initial removal of Na⁺ from the 4h position. This signal becomes unique, showing an almost-single Na environment corresponding to the 2c position after removal of 0.55 Na⁺ (spectrum III in Fig. 4d). Afterwards, the signal (shifted to lower chemical shifts of 1,300 ppm) is also broadened (800 versus 250–500 ppm) signifying a considerable increase in the local disorder around the remaining sodium ions (roughly 0.09 Na⁺ per formula unit at full charge), most probably linked to the onset of O₂ release (between points III and IV in Fig. 4a according to the OEMS measurement). Moreover, the existence of a very broad peak is also compatible with the slow Na⁺ dynamics, which

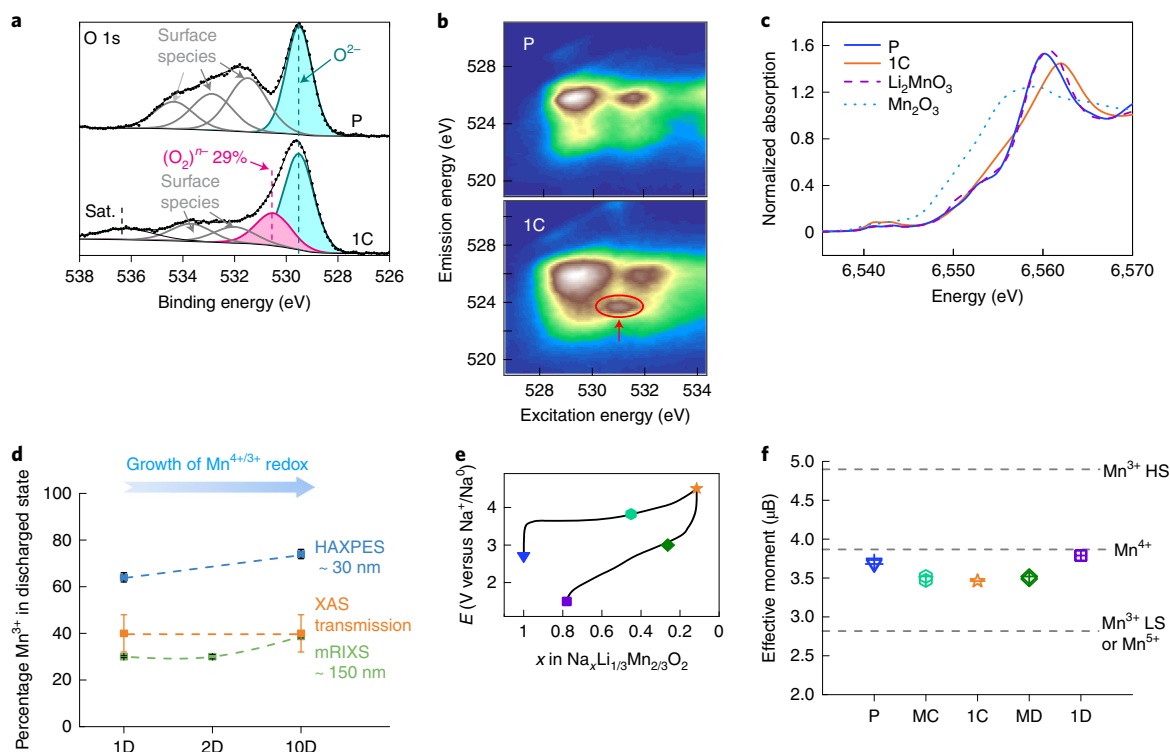


Fig. 5 | Charge compensation mechanism in $\text{NaLi}_{1/3}\text{Mn}_{2/3}\text{O}_2$. **a, b**, Ex situ HAXPES ($h\nu = 6,900$ eV) O1s (**a**) and ex situ O K-edge mRIXS spectra (**b**) of pristine (P) and charged to 4.5 V samples (1C). Red arrow and circle at 531.0 eV excitation energy and 523.7 eV emission energy indicate the oxidized oxygen feature at a fully charged state. Sat., an extra satellite peak that has been previously observed³¹. **c**, Mn K-edge XANES spectra of pristine (blue solid) and sample charged to 4.5 V (orange solid), compared to references of Mn^{4+} (purple dashed) and Mn^{3+} (cyan dotted). **d**, Concentration of Mn^{3+} species derived from ex situ HAXPES, mRIXS and XAS in the first, second and tenth discharged (1.5 V) samples. **e**, First cycle charge-discharge curve with points indicating the state of charge or discharge at which ex situ samples for magnetic measurements were extracted from. **f**, Effective magnetic moment deduced from magnetic susceptibility measurements. P, MC, 1C, MD and 1D represents pristine, mid-charge, first charge, mid-discharge and first discharge samples, respectively. Dashed lines indicate theoretical values of spin-only effective magnetic moments (μ_{eff}) of Mn at different oxidation states and spin states. μ_{eff} shows a valley-like behaviour on discharge while the reduction of Mn^{4+} to Mn^{3+} according to spectroscopy techniques should lead to an obvious increase.

prevents the averaging of the shift, and may explain the hysteresis observed in GITT measurements at high potential. On discharge, the reinsertion of Na^+ leads to a very broad ($>1,300$ ppm) Gaussian distribution of environments, indicative of a massive structural disorder resulting from a broader distribution of Na–O–Mn angles that govern the NMR shifts²⁹. The ^{23}Na NMR spectrum after a second cycle (Supplementary Fig. 20) shows a broad line at 910 ppm that is half as wide (650 ppm) as at the end of the first discharge, indicating that some local order is restored during the second cycle. Consistently, similar broad ^{23}Na NMR signals were previously reported for the fully charged $\text{Na}_x\text{Ni}_{0.5}\text{Mn}_{0.5}\text{O}_2$ phase with disordered Na occupation³⁰.

Altogether, NMR results show that on Na^+ removal, $\text{Na}_x\text{Li}_{1/3}\text{Mn}_{2/3}\text{O}_2$ undergoes a partially irreversible migration of Li^+ to the Na layers that creates cation vacancies and disorder within the metal layers. Due to such an intense modification of the structure, some of the Na^+ can no longer return to their initial sites, which are irreversibly occupied by 0.25 lithium ions (explaining the irreversible loss of 0.23 Na during the first charge/discharge cycle). Therefore, they will occupy sites having different environments, explaining the broadened spectra.

During the first charge of $\text{NaLi}_{1/3}\text{Mn}_{2/3}\text{O}_2$, a combination of X-ray absorption (XAS), hard X-ray photoelectron spectroscopy (HAXPES) and mapping of resonant inelastic X-ray scattering (mRIXS) show features related solely to oxygen oxidation at various depths (particle size of >0.5 μm , Supplementary Fig. 21). A new

peak at the binding energy of 530.5 eV emerges on full charge in the O1s HAXPES (Fig. 5a and Supplementary Figs. 22 and 23, left), and is assigned to oxidized lattice oxygen O^{n-} ($n < 2$)³¹. This oxygen activity is unambiguously confirmed by the appearance of an additional feature in mRIXS (see the ellipse in Fig. 5b), at excitation and emission energies of 531.0 and 523.7 eV, respectively, characteristic of O^{n-} (ref. ³²). These features appear and disappear during charge-discharge, confirming the reversibility of the anionic process (Supplementary Fig. 24).

Moreover, all the spectroscopic techniques consistently indicate that Mn^{4+} is redox inactive on first charge (Supplementary Figs. 22 and 25–28). In contrast, on discharge, they show a varying degree of reduction from Mn^{4+} to Mn^{3+} depending on the depth sensitivity of the technique used (Fig. 5d and Supplementary Figs. 22 and 25–28). HAXPES indicates nearly 64% of Mn^{3+} at the surface (roughly 30 nm probing depth) of the fully discharged electrode, compared to just around 30% measured by mRIXS, which has a probing depth of around 150 nm. The Mn K-edge XAS measurements in transmission mode are closer to picture the whole cell electrode, which is roughly 40 μm thick. Quantification via linear combinations of references was not possible due to the lack of adequate standards to reflect the changes in position and shape of the Mn K-edge spectra with formal oxidation state and coordination environment³³. Instead, a calibration curve was built from standards of different oxidation states using the spectral integration proposed by Dau et al.³⁴, rendering an approximate average state of roughly 3.6+ for

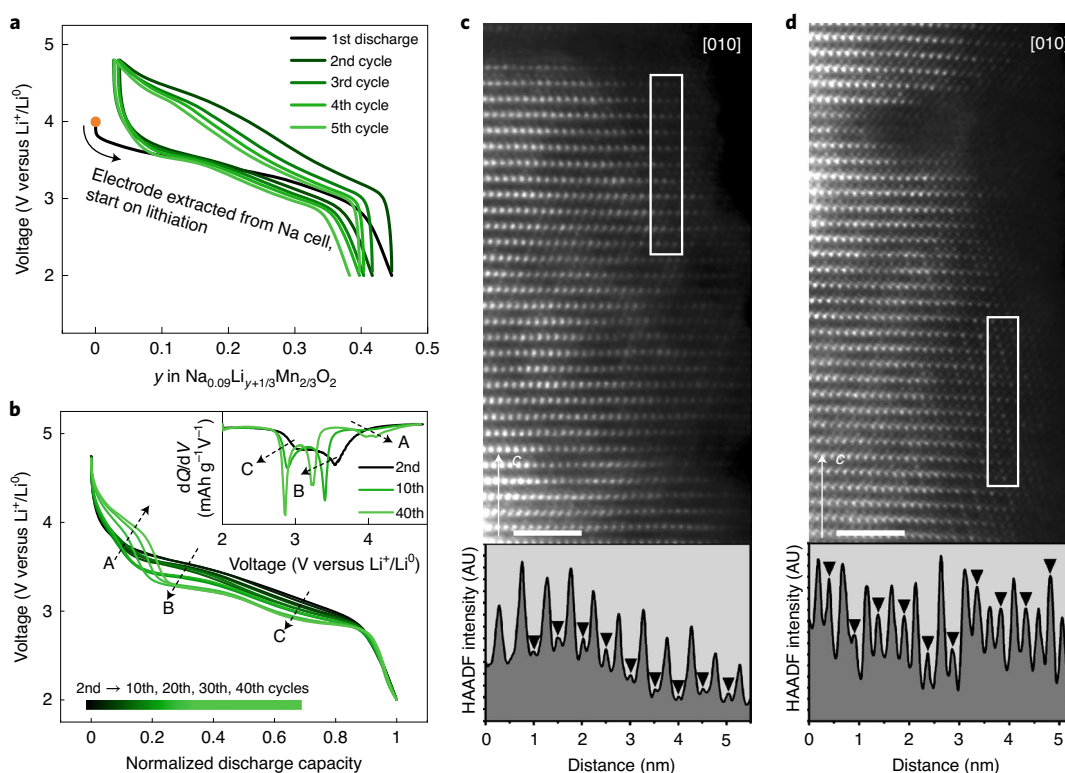


Fig. 6 | Voltage fade and cation migration in Li half cells. a, First five cycles of voltage-composition profiles of the desodiated $\text{Na}_{0.09}\text{Li}_{1/3}\text{Mn}_{2/3}\text{O}_{1.86}$ electrode cycled in Li half cells with an 1M LiPF_6 in EC-DMC (vol/vol = 50/50, LP30) electrolyte. **b**, Normalized discharge curves of the same cell for 40 cycles with dQ/dV of selected cycles, showing the evolution of low voltage redox process and voltage fade on cycling in the Li cell. The actual discharge profile before normalization is given in Supplementary Fig. 30. **c,d**, The [010] HAADF-STEM images and corresponding HAADF intensity profiles show increasing cation migration from the first discharged sample (**c**) to the tenth discharged sample (**d**) in the Li cell. The peaks in the HAADF intensity profiles (bottom) correspond to the Mn columns at the metal layers, whereas the intensity between the peaks (marked with black arrowheads) indicates the migration of the Mn cations into the interlayer space. Scale bars, 2 nm.

the discharged (1D) sample (Supplementary Fig. 27), consistent with mRIXS (Supplementary Fig. 26 and Fig. 5d). Last, the changes in Mn spectra were reproduced on extensive cycling, proving that the $\text{Mn}^{4+/3+}$ redox couple was permanently activated after the first charge (Supplementary Figs. 23 and 25–27).

Alternatively, to further probe the oxidation state of Mn, ex situ magnetic susceptibility measurements were carried out from 2 to 400 K on $\text{Na}_x\text{Li}_{1/3}\text{Mn}_{2/3}\text{O}_2$ samples at various states of charge and discharge (Fig. 5f). An effective magnetic moment (μ_{eff}) of roughly $3.70 \mu_B$ is measured for the pristine sample, hence confirming the presence of Mn^{4+} . However, given the substantial amount of Mn^{3+} determined by spectroscopy, the small increase of μ_{eff} in the discharge sample (Supplementary Fig. 29 and Supplementary Table 7) compared to the pristine one (3.79 versus $3.70 \mu_B$) strongly suggests internal charge transfer between Mn and O during oxidation. This indirectly supports the participation of anions in the redox activity of $\text{NaLi}_{1/3}\text{Mn}_{2/3}\text{O}_2$, as corroborated by our recent theoretical calculations on $\text{Na}_{2/3}[\text{Mg}_{1/3}\text{Mn}_{2/3}]_2$ (ref. 35) showing that the coupling of unpaired electrons on both Mn and O decreases the total magnetization of the cell. However, it is beyond the scope of this paper to quantitatively decouple the Mn from the O contribution for μ_{eff} values.

Last, we check the electrochemical reactivity of the nearly Na-free electrode $\text{Na}_{0.09}\text{Li}_{1/3}\text{Mn}_{2/3}\text{O}_2$ against Li by assembling a $\text{Na}_{0.09}\text{Li}_{1/3}\text{Mn}_{2/3}\text{O}_2/\text{Li}$ cell. Its voltage profile (Fig. 6a) shows the reversible uptake of 0.4 Li^+ per formula unit together with good capacity retention on cycling, yet accompanied by large voltage decay (Fig. 6b). From combined Coulombic titration and ICP-OES

analysis, the chemical composition of the fully discharged sample was identified as $\text{Na}_{0.09}\text{Li}_{0.73}\text{Mn}_{0.67}\text{O}_2$. Mn migration on Li insertion was evidenced by TEM. The [010] HAADF-STEM images and corresponding intensity profiles are reported after one (Fig. 6c) and ten (Fig. 6d) charge-discharge cycles in Li-ion half cells. The outlined rectangular areas reveal the Mn cation migrations that are enhanced with cycling. Note that the Mn migration is more pronounced in the sample after ten cycles, which indicates only a partially reversible character of this migration. This drastically contrasts with similar images taken on the material cycled versus Na in Na-based electrolytes where no Mn migration towards the alkali layers can be spotted (Fig. 3).

Altogether, our study reports a new anionic redox active $\text{O3-NaLi}_{1/3}\text{Mn}_{2/3}\text{O}_2$ phase that shows neither voltage fade nor interlayer cation migration when cycled against Na, while it does with Li. Therefore, it provides valuable information for clarifying the complex interplay between anionic redox, cationic migration, voltage hysteresis and voltage fade in layered $3d$ transition metal oxides.

First, to rationalize the Li/Na competition occurring through the Na removal in $\text{O3-NaLi}_{1/3}\text{Mn}_{2/3}\text{O}_2$, DFT calculations were performed on the $C2/m$ structural model of multiple variations for partially charged $\text{O3-Na}_x\text{Li}_{1/3}\text{Mn}_{2/3}\text{O}_2$ structures with the Li^+/Na^+ cations distributed over three crystallographic positions $2b$ (metal layer) and $4h, 2c$ (alkali layer). We found that all O3 configurations with partial or total Li migration to the alkali layer, namely Li(M+A) or Li(A) are substantially destabilized against those having Li in the metal layer, namely Li(M) up to the removal of $1/3 \text{ Na}^+$. Through this domain, the computed average potential (3.5 V) is in fair agreement

with experiments (Supplementary Table 8). However, this energy penalty for Li migration to the alkali layer is removed on further Na^+ extraction as $\text{Li}(\text{M}+\text{A})$ and $\text{Li}(\text{A})$ configurations become equally or more stable than $\text{Li}(\text{M})$ configurations at Na concentration $x_{\text{Na}} = 1/3$ and $1/6$, respectively. The presence of Li in the alkali layer leads to a contraction of the c lattice parameter, consistent with the crystallographic features of $\text{O3}(\text{II})$ (Supplementary Table 8). This size-constrained alkali interlayer could kinetically hinder the additional removal of Na^+ from the $x_{\text{Na}} = 1/3$ phase, hence leading to the voltage polarization observed in the galvanostatic curve of Fig. 2 along the second process. Note that O_2 release is triggered when nearly all Li has moved to the alkali layers. This observation is not fortuitous since Li migration to the alkali layer indicates that some oxygen atoms become less electrostatically bonded to the structural network due to cationic vacancies in their local environment and therefore more prone to oxidation. It is noteworthy that the presence of Li vacancies in the metal layer may also favour $\text{Mn}/\square_{\text{cat}}$ disorder in the metal layer, as observed in the SXRD and STEM data.

Besides, first-principles DFT calculations have also shown (Supplementary Table 9) that Mn migration from the metal to the alkali layer is thermodynamically less favoured (by at least 200–300 meV per Mn) when the alkali layer contains Na. This confirms the absence of Mn migration deduced by SXRD and STEM data. Moreover, it indicates that the presence of Na^+ ions in the alkali layer, even in small amounts, imposes a too large interlayer spacing to stabilize Mn^{4+} in the octahedral site. In contrast, the c parameter for pure Li phases is systematically smaller by at least 1.5 \AA , which again confirms the greater ability of Li-based phases to stabilize the Mn cations in the interlayer space. Thus, it does not come as a surprise that Li insertion in $\text{O3-Na}_{0.09}\text{Li}_{1/3}\text{Mn}_{2/3}\text{O}_2$ behaves similarly to the pure Li phases, as Li^+ occupies positions in both alkali and metal layers.

In absence of Mn migration to the alkali layer in $\text{NaLi}_{1/3}\text{Mn}_{2/3}\text{O}_2$, we could hastily eliminate the densification hypothesis before realizing that Mn migration within the metal layers could be an alternative way to trigger densification as explained below. Let us first recall that the complete migration of Li^+ cations from the $[\text{Li}_{1/3}\text{Mn}_{2/3}]\text{O}_2$ layer to the alkali layer on the first charge leaves cationic vacancies: $\text{Na}_{0.09}\text{Li}_{1/3}[(\square_{\text{cat}})_{1/3}\text{Mn}_{2/3}]\text{O}_{1.86}$. Realization of oxygen deficiency through anion vacancies should lower the coordination number of Mn below six, but Mn K-edge X-ray absorption near edge structure (XANES) spectra and extended X-ray absorption fine structure spectrometry reveal octahedral Mn coordination at all states of charge. Thus, the oxygen vacancies must be eliminated by migration from the bulk to surface and the increasing Mn to O ratio is accommodated by intralayer Mn^{4+} cation migration to vacant cation sites \square_{cat} . The chemical formula at full charge can be recast as $\text{Na}_{0.09}\text{Li}_{0.36}[(\square_{\text{cat}})_{0.28}\text{Mn}_{0.72}]\text{O}_2$. Disrupting the 1:2 (\square_{cat}):Mn ratio should suppress the honeycomb cation ordering and promote a stochastic arrangement of Mn^{4+} and cation vacancies in the densified $[(\square_{\text{cat}})_{0.28}\text{Mn}_{0.72}]\text{O}_2$ layers, as indicated by the vanishing intensity of the honeycomb superlattice reflections in the SXRD patterns (Fig. 3a) and confirmed by DFT calculations (Supplementary Table 9).

From a more general perspective, the study of $\text{O3-NaLi}_{1/3}\text{Mn}_{2/3}\text{O}_2$ comforts the robustness of the interplay between cationic migration and voltage fade- O_2 release with an additional fine-tuning that distinguishes in- or out-plane migration. Indeed, the $\text{O3-NaLi}_{1/3}\text{Mn}_{2/3}\text{O}_2$ exemplifies very clearly that if the densification after first oxygen release occurs through the intralayer transition metal cation migration, the material demonstrates virtually no voltage fade, whereas switching to the interlayer migration mode (for example, cycling versus Li^+/Li^0) readily introduces voltage fade. Besides showing no discernible voltage fade, $\text{O3-NaLi}_{1/3}\text{Mn}_{2/3}\text{O}_2$ offers other positive attributes such as a reversible capacity of 190 mAh g^{-1} associated with a good capacity retention while showing robust water stability, which is rare for stoichiometric Na-based layered compounds.

However, such benefits when considering applications are tarnished by the large voltage hysteresis displayed by the $\text{O3-NaLi}_{1/3}\text{Mn}_{2/3}\text{O}_2$ electrode that we propose to be due to intralayer Mn migration. We are trying to contour this roadblock via the injection of a robust ordering scheme within the transition metal layer. We hope these findings help in providing a way towards the design of anionic redox active O3-type Na phases with higher energy efficacy.

Online content

Any methods, additional references, Nature Research reporting summaries, source data, extended data, supplementary information, acknowledgements, peer review information; details of author contributions and competing interests; and statements of data and code availability are available at <https://doi.org/10.1038/s41563-020-00870-8>.

Received: 22 April 2020; Accepted: 3 November 2020;

Published online: 11 January 2021

References

- Tarascon, J. M. The Li-ion battery: 25 years of exciting and enriching experiences. *Electrochem. Soc. Interface* **25**, 79–83 (2016).
- Yabuuchi, N., Kubota, K., Dahbi, M. & Komaba, S. Research development on sodium-ion batteries. *Chem. Rev.* **114**, 11636–11682 (2014).
- Hwang, J.-Y., Myung, S.-T. & Sun, Y.-K. Sodium-ion batteries: present and future. *Chem. Soc. Rev.* **46**, 3529–3614 (2017).
- Rozier, P. & Tarascon, J. M. Review—Li-rich layered oxide cathodes for next-generation Li-ion batteries: chances and challenges. *J. Electrochem. Soc.* **162**, A2490–A2499 (2015).
- Lu, Z. & Dahn, J. R. Understanding the anomalous capacity of $\text{Li}/\text{Li}[\text{Ni}_x\text{Li}_{1/3-2x/3}\text{Mn}_{2/3-x/3}]\text{O}_2$ cells using in situ X-ray diffraction and electrochemical studies. *J. Electrochem. Soc.* **149**, A815–A822 (2002).
- Thackeray, M. M., Johnson, C. S., Vaughey, J. T., Li, N. & Hackney, S. A. Advances in manganese-oxide ‘composite’ electrodes for lithium-ion batteries. *J. Mater. Chem.* **15**, 2257–2267 (2005).
- Xie, Y., Saubanère, M. & Doublet, M.-L. Requirements for reversible extra-capacity in Li-rich layered oxides for Li-ion batteries. *Energy Environ. Sci.* **10**, 266–274 (2017).
- Ben Yahia, M., Vergnet, J., Saubanère, M. & Doublet, M.-L. Unified picture of anionic redox in Li/Na-ion batteries. *Nat. Mater.* **18**, 496–502 (2019).
- Rozier, P. et al. Anionic redox chemistry in Na-rich $\text{Na}_2\text{Ru}_{1-y}\text{Sn}_y\text{O}_3$ positive electrode material for Na-ion batteries. *Electrochem. Commun.* **53**, 29–32 (2015).
- Assadi, M. H. N., Okubo, M., Yamada, A. & Tateyama, Y. Oxygen redox promoted by Na excess and covalency in hexagonal and monoclinic $\text{Na}_{2-x}\text{RuO}_3$ polymorphs. *J. Electrochem. Soc.* **166**, A5343–A5348 (2019).
- Mortemard de Boisse, B. et al. Intermediate honeycomb ordering to trigger oxygen redox chemistry in layered battery electrode. *Nat. Commun.* **7**, 11397 (2016).
- Perez, A. J. et al. Strong oxygen participation in the redox governing the structural and electrochemical properties of Na-rich layered oxide Na_2IrO_3 . *Chem. Mater.* **28**, 8278–8288 (2016).
- Zhang, X. et al. Manganese-based Na-rich materials boost anionic redox in high-performance layered cathodes for sodium-ion batteries. *Adv. Mater.* **31**, 1807770 (2019).
- House, R. A. et al. Superstructure control of first-cycle voltage hysteresis in O-redox cathodes. *Nature* **577**, 502–508 (2020).
- Maitra, U. et al. Oxygen redox chemistry without excess alkali-metal ions in $\text{Na}_{2/3}[\text{Mg}_{0.28}\text{Mn}_{0.72}]\text{O}_2$. *Nat. Chem.* **10**, 288–295 (2018).
- Du, K. et al. Exploring reversible oxidation of oxygen in a manganese oxide. *Energy Environ. Sci.* **9**, 2575–2577 (2016).
- Rong, X. et al. Anionic redox reaction-induced high-capacity and low-strain cathode with suppressed phase transition. *Joule* **3**, 503–517 (2019).
- Bai, X. et al. Anionic redox activity in a newly Zn-doped sodium layered oxide $\text{P2-Na}_{2/3}\text{Mn}_{1-y}\text{Zn}_y\text{O}_2$ ($0 < y < 0.23$). *Adv. Energy Mater.* **8**, 1802379 (2018).
- Bai, X., Iadecola, A. & Tarascon, J.-M. & Rozier, P. Decoupling the effect of vacancies and electropositive cations on the anionic redox processes in Na based P2-type layered oxides. *Energy Storage Mater.* **31**, 146–155 (2020).
- Ma, C. et al. Exploring oxygen activity in the high energy P2-type $\text{Na}_{0.78}\text{Ni}_{0.23}\text{Mn}_{0.69}\text{O}_2$ cathode material for Na-ion batteries. *J. Am. Chem. Soc.* **139**, 4835–4845 (2017).
- Mariyappan, S., Wang, Q. & Tarascon, J. M. Will sodium layered oxides ever be competitive for sodium ion battery applications? *J. Electrochem. Soc.* **165**, A3714–A3722 (2018).

22. Kim, D., Cho, M. & Cho, K. Rational design of $\text{Na}(\text{Li}_{1/3}\text{Mn}_{2/3})\text{O}_2$ operated by anionic redox reactions for advanced sodium-ion batteries. *Adv. Mater.* **29**, 1701788 (2017).
23. Perez, A. J., Rousse, G. & Tarascon, J.-M. Structural instability driven by Li/Na competition in $\text{Na}(\text{Li}_{1/3}\text{Ir}_{2/3})\text{O}_2$ cathode material for Li-ion and Na-ion batteries. *Inorg. Chem.* **58**, 15644–15651 (2019).
24. de la Llave, E. et al. Improving energy density and structural stability of manganese oxide cathodes for Na-ion batteries by structural lithium substitution. *Chem. Mater.* **28**, 9064–9076 (2016).
25. House, R. A. et al. What triggers oxygen loss in oxygen redox cathode materials? *Chem. Mater.* **31**, 3293–3300 (2019).
26. Grey, C. P. & Lee, Y. J. Lithium MAS NMR studies of cathode materials for lithium-ion batteries. *Solid State Sci.* **5**, 883–894 (2003).
27. Lee, Y. J. & Grey, C. P. Determining the lithium local environments in the lithium manganates $\text{LiZn}_{0.5}\text{Mn}_{1.5}\text{O}_4$ and Li_2MnO_3 by analysis of the ^6Li MAS NMR spinning sideband manifolds. *J. Phys. Chem. B.* **106**, 3576–3582 (2002).
28. Shimoda, K. et al. Direct observation of layered-to-spinel phase transformation in Li_2MnO_3 and the spinel structure stabilised after the activation process. *J. Mater. Chem. A.* **5**, 6695–6707 (2017).
29. Clément, R. J. et al. Direct evidence for high Na^+ mobility and high voltage structural processes in $\text{P2-Na}_x[\text{Li}_y\text{Ni}_z\text{Mn}_{1-y-z}]\text{O}_2$ ($x, y, z \leq 1$) cathodes from solid-state NMR and DFT calculations. *J. Mater. Chem. A.* **5**, 4129–4143 (2017).
30. Cabana, J. et al. Study of the transition metal ordering in layered $\text{Na}_x\text{Ni}_{x/2}\text{Mn}_{1-x/2}\text{O}_2$ ($2/3 \leq x \leq 1$) and consequences of Na/Li exchange. *Inorg. Chem.* **52**, 8540–8550 (2013).
31. Assat, G. et al. Fundamental interplay between anionic/cationic redox governing the kinetics and thermodynamics of lithium-rich cathodes. *Nat. Commun.* **8**, 2219 (2017).
32. Dai, K. et al. High reversibility of lattice oxygen redox quantified by direct bulk probes of both anionic and cationic redox reactions. *Joule* **3**, 518–541 (2019).
33. Ito, A. et al. In situ X-ray absorption spectroscopic study of Li-rich layered cathode material $\text{Li}[\text{Ni}_{0.17}\text{Li}_{0.2}\text{Co}_{0.07}\text{Mn}_{0.56}]\text{O}_2$. *J. Power Sources* **196**, 6828–6834 (2011).
34. Dau, H., Liebisch, P. & Haumann, M. X-ray absorption spectroscopy to analyze nuclear geometry and electronic structure of biological metal centers—potential and questions examined with special focus on the tetra-nuclear manganese complex of oxygenic photosynthesis. *Anal. Bioanal. Chem.* **376**, 562–583 (2003).
35. Vergnet, J., Saubanère, M., Doublet, M.-L. & Tarascon, J.-M. The structural stability of P2-layered Na-based electrodes during anionic redox. *Joule* **4**, 420–434 (2020).

Publisher's note Springer Nature remains neutral with regard to jurisdictional claims in published maps and institutional affiliations.

© The Author(s), under exclusive licence to Springer Nature Limited 2021

Methods

Synthesis. Here, 415 mg of Na_2O_2 (Alfa Aesar, 95%), 53 mg of Li_2O (Alfa Aesar, 99.5%) and 560 mg of Mn_2O_3 (Sigma Aldrich, 99%) were thoroughly mixed in a mortar before being placed in an alumina boat. The boat was placed in a quartz tube of 62 cm in length and 32 mm in diameter that was then put in a tubular furnace (type carbolite) with a 30-cm heating zone. After placing the sample, the alumina tube was flushed with argon for 45 min with an Ar flow of 50 ml min^{-1} . Then, the argon flow was stopped and the sample was heated to 700°C for 8 h and then cooled down to room temperature. The as-synthesized material was soaked in distilled water (100 mg per 10 ml of H_2O) while sonicating for 30 min followed by drying at 80°C under vacuum overnight.

Electrochemical characterization. Electrochemical characterization was carried out in Swagelok-type cells versus metallic Na, with 1 M NaPF_6 (Stella Chemifa) dissolved in propylene carbonate (PC) as the electrolyte and a Whatman GF/D borosilicate glass fibre membrane as a separator. The cathode material was used in the form of a self-standing film electrode comprising 76 wt% active material, 20 wt% carbon Super P (Csp) and 4 wt% polytetrafluoroethylene (PTFE). Typical loading of cathode active materials was around 5 mg cm^{-2} . All cells were assembled in an Ar-filled glovebox and were cycled in galvanostatic mode at current rates ranging from C/8 to C/20 (1 Na^+ exchanged in 8–20 h). GITT measurement was performed in the second cycle of $\text{NaLi}_{1/3}\text{Mn}_{2/3}\text{O}_2/\text{Na}$ cells at 25°C with steps of 0.2 Na^+ exchange and OCV period of 20 h.

For cycling versus metallic Li, a nearly Na-free electrode, $\text{Na}_{0.06}\text{Li}_{1/3}\text{Mn}_{2/3}\text{O}_2$ was recovered and washed from a $\text{NaLi}_{1/3}\text{Mn}_{2/3}\text{O}_2/\text{Na}$ Swagelok cell that was fully charged to 4.5 V versus Na^+/Na , before being used in a new Swagelok with Li metal as a negative electrode and 1 M LiPF_6 in ethylene carbonate (EC)-dimethyl carbonate (DMC) (vol/vol = 50/50, LP30) as electrolyte. The Li cells are also cycled at current rates ranging from C/8 to C/20 at 25°C .

To prepare ex situ samples for characterization, the cathode consisted of either PTFE film (XAS, mRIXS) as described before, or a powder composite of active material mixed with 15–25 wt% Csp (SXR, TEM, NMR, HAXPES, SQUID and ICP-OES). Ex situ samples were extracted from the cycled cells in an Ar-filled glovebox and washed in DMC five times before sealing and transferring under Ar.

Gas analysis. For pressure analysis and OEMS measurements, we used $\text{Na}_3\text{V}_2(\text{PO}_4)_3$ as a counter electrode to avoid gas generation from side reactions with common anode materials such as Na and hard carbon. The $\text{NaLi}_{1/3}\text{Mn}_{2/3}\text{O}_2$ and $\text{Na}_3\text{V}_2(\text{PO}_4)_3$ (NVP) were both used in the form of a self-standing electrode (76% active material, 20% Csp, 4% PTFE). One piece of GF/D glass fibre was used as a separator. In-house pressure cells or OEMS cells were assembled in an Ar-filled glovebox and then cycled at C/20 current rate (0.05 Na^+ exchange per h for $\text{NaLi}_{1/3}\text{Mn}_{2/3}\text{O}_2$) with 150 μl of electrolyte (1 M NaPF_6 dissolved in PC) and cut-off potentials of -0.5 – 3.1 V versus NVP. The OEMS and pressure cell setup is described elsewhere^{36,37}. For OEMS, gaseous products were collected and analysed using the LabView program.

XRD. XRD patterns were performed on pristine samples using a BRUKER D8 Advance diffractometer equipped with $\text{Cu K}\alpha$ radiation source ($\lambda \text{ K}\alpha_1 = 1.54056 \text{ \AA}$, $\lambda \text{ K}\alpha_2 = 1.54439 \text{ \AA}$). Operando XRD was carried out on the same diffractometer in an electrochemical cell equipped with a binding energy window. SXR was performed on pristine and ex situ powders at the 11-BM beamline (Advanced Photon Source, Argonne National Laboratory). Rietveld refinement on the XRD patterns were conducted using the FullProf Suite³⁸. Simulation of stacking faults in the pristine sample was done using the FAULTS software available in the FullProf Suite³⁹.

TEM. The samples were prepared by crushing the crystals with an agate mortar and pestle in DMC and depositing drops of suspension onto a carbon film supported by a copper grid. Samples for TEM were stored and prepared in an Ar-filled glovebox. A special Gatan vacuum transfer holder was used for analyses and transportation of the samples from the Ar-filled glovebox to the TEM column to prevent interaction with air. SAED patterns and HAADF-STEM images were acquired on a probe aberration-corrected FEI Titan Themis Z transmission electron microscope operated at 200 kV.

NPD. Neutron diffraction data were collected at the ECHIDNA high-resolution powder diffractometer at the OPAL research facility (Lucas Heights, Australia)⁴⁰. Three samples were filled into thin-wall vanadium containers with a wall thickness of 150 μm and 10 mm in diameter, and sealed under argon with indium metal wire. Data collection was performed at ambient temperature in Debye-Scherrer geometry under constant spinning. Monochromatic neutrons were obtained at a (533) reflection of a composite vertically focusing Ge monochromator at a 140° take-off angle. A wavelength $\lambda = 1.622043(15) \text{ \AA}$ was determined using the full-profile refinement of LaB_6 reference from the National Institute of Standards and Technology. Diffraction data were obtained in the 2θ range (4 – 164°) using 25 resolution steps of the 2D multidetector consisting of 128 ^3He vertical positionally sensitive tubes. The exposure time was 9 h per dataset and equal for the samples studied. All patterns were refined by the Rietveld method using the FullProf suite⁴¹.

ICP-OES. ICP-OES was performed to determine the elemental compositions of the material before and after H_2O treatment and electrochemical cycling with a ThermoFisher iCAP 6000 device. All powders were first digested in aqua regia, followed by a filtering process for the cycled samples to remove the conductive carbon in the composite electrodes.

NMR. Solid-state NMR experiments were performed on a 4.7T Avance III HD Bruker NMR spectrometer (200 MHz for ^1H , 29.4 MHz for ^6Li and 52.9 MHz for ^{23}Na), using a 1.3 mm magic angle spinning (MAS) probe spinning at 62.5 kHz under pure nitrogen gas. Without temperature regulation, the temperature inside the rotor is expected to be around 50°C .

All experiments were recorded with a rotor-synchronized Hahn echo sequence. For the ^6Li spectra, the 90° pulse was set to 1.11 μs and the chemical shift was referenced with liquid $^6\text{LiCl}$ in water (corresponding to a 225 kHz B_1 field strength). For ^{23}Na spectra, the Hahn echo was recorded with a 45° – τ – 90° – τ sequence to account for the quadrupolar effect, using a 1.47- μs long, low power 45° radiofrequency (RF) pulse (corresponding to a 85 kHz B_1 field strength). To ensure optimal detection of the signals affected by quadrupolar broadening, several experiments were performed with RF powers ranging between 50 and 5 W, and the RF power was set at 12.5 W to avoid any loss of signal. Moreover, to ensure proper detection and phasing of the broad signal for discharged samples and avoid baseline distortion issues, a full echo signal was also acquired after a first evolution delay of 16 rotor periods⁴². The resulting full echo signal has the same lineshape as the conventional Hahn echo signal after proper phasing, thereby confirming the first results. All T_1 relaxation times were measured in the 500 μs –10 ms range, and therefore, all spectra were recorded with a 50-ms recycling delay ensuring full recovery of the magnetization. No spinning sideband were detected in our experiments thanks to the low-field/high spinning speed combination.

The 1.3-mm zirconia rotor was filled inside a glovebox under argon, and the rotor was weighted before and after the filling procedure to obtain the sample mass (around 2.7–4.6 mg). Depending on the sensitivity of the experiments, the total number of recorded transients varied between 32,768 and 1,403,472 and MAS was performed under dry N_2 gas. The spectra were deconvoluted with dmfit⁴³. Special care was taken to measure NMR spectra on fresh samples with as little contact as possible with residual moisture in the glovebox or in the NMR spectrometer. Contact with moisture results in the quick evolution of NMR spectra, with sharper peaks appearing in the 0–300 ppm range in ^{23}Na NMR spectra, as noticed previously²⁹.

HAXPES. HAXPES measurements were performed at the GALAXIES beamline of synchrotron SOLEIL (France)⁴⁴, using photon excitation energy of 6,900 eV obtained from the third-order reflections of the Si(111) crystal monochromator. Photoelectrons were analysed by a SCIENTA EW4000 spectrometer, and the obtained energy resolution from the Au Fermi edge was 0.14 eV for 6,900 eV photon energy. No charge neutralization was used and the analysis chamber was under a high vacuum of roughly 10^{-11} bar during the measurements.

mRIXS. mRIXS was measured in the iRIXS endstation at Beamline 8.0.1 at the Advanced Light Source, Lawrence Berkeley Laboratory⁴⁵. Further experimental details are exhibited in Supplementary Note 1.

XAS. Ex situ and operando XAS measurements at the Mn K-edge were performed in transmission mode at the ROCK beamline⁴⁶ at Synchrotron SOLEIL in France. Further details of the experiments and data analyses are included in Supplementary Note 2.

Magnetic measurements. Susceptibility measurements were conducted in a zero-field cooling mode using a SQUID XL magnetometer (Quantum design), under applied magnetic fields of 1 T in a temperature range of 2–400 K. The powder samples were sealed in quartz tubes under vacuum to avoid any contact with air. A small piece of cotton was used to prevent the motion of the powders along the quartz tube. Both the quartz tube and cotton have been found to be transparent to magnetic measurements.

DFT. Spin-polarized DFT calculations were performed using the plane-wave DFT Vienna Ab initio Simulation Package code^{47,48} within the generalized gradient approximation of Perdew–Burke–Ernzerhof to describe electron exchange and correlation⁴⁹.

The rotationally invariant Dudarev method (DFT+U)⁵⁰ was used to correct the self-interaction error of conventional DFT for correlated d electrons with $U_{\text{eff}} = 4 \text{ eV}$ for Mn. Various Li/Na configurations were tested with alkali lying in the 2b, 2c or 4h Wyckoff positions of the $C2/m$ model structure. Mn migration was investigated in $2 \times 1 \times 1$ super cells (eight Mn per cell). All atom coordinates and lattice parameters were fully relaxed using conjugate gradient energy minimization until the forces acting on each atom were lower than $5 \times 10^{-3} \text{ eV \AA}^{-2}$. A plane-wave cut-off of 600 eV was used to define the basis set, with well-converged k -point sampling for each compound. Both ferromagnetic and antiferromagnetic arrangements were considered in the calculation, the former leading generally to slightly more stable structures within one or two $k_B T$ (room temperature activation energy roughly 25 meV). Madelung potentials were computed using home-made code.

Data availability

All relevant data are included in the article and its Supplementary Information.

References

- Berg, E. J. & Novák, P. Recent progress on Li-O₂ batteries at PSI. in *ECL Annual Report* (Paul Scherrer Institut, 2012).
- Lepoivre, F., Grimaud, A., Larcher, D. & Tarascon, J.-M. Long-time and reliable gas monitoring in Li-O₂ batteries via a swagelok derived electrochemical cell. *J. Electrochem. Soc.* **163**, A923–A929 (2016).
- FullProf Suite (Full Prof Team, 2006); <https://www.ill.eu/sites/fullprof/>
- Casas-Cabanas, M., Reynaud, M., Rikarte, J., Horbach, P. & Rodríguez-Carvajal, J. FAULTS: a program for refinement of structures with extended defects. *J. Appl. Cryst.* **49**, 2259–2269 (2016).
- Avdeev, M. & Hester, J. R. ECHIDNA: a decade of high-resolution neutron powder diffraction at OPAL. *J. Appl. Cryst.* **51**, 1597–1604 (2018).
- Rodríguez-Carvajal, J. Recent advances in magnetic structure determination by neutron powder diffraction. *Phys. B.* **192**, 55–69 (1993).
- Grandinetti, P. J. et al. Pure-absorption-mode lineshapes and sensitivity in two-dimensional dynamic-angle spinning NMR. *J. Magn. Reson. A* **103**, 72–81 (1993).
- Massiot, D. et al. Modelling one- and two-dimensional solid-state NMR spectra. *Magn. Reson. Chem.* **40**, 70–76 (2002).
- Rueff, J.-P. et al. The GALAXIES beamline at the SOLEIL synchrotron: inelastic X-ray scattering and photoelectron spectroscopy in the hard X-ray range. *J. Synchrotron Rad.* **22**, 175–179 (2015).
- Qiao, R. et al. High-efficiency in situ resonant inelastic X-ray scattering (iRIXS) endstation at the Advanced Light Source. *Rev. Sci. Instrum.* **88**, 033106 (2017).
- Briois, V. et al. ROCK: the new Quick-EXAFS beamline at SOLEIL. *J. Phys. Conf. Ser.* **712**, 012149 (2016).
- Kresse, G. & Hafner, J. Ab initio molecular dynamics for liquid metals. *Phys. Rev. B.* **47**, 558–561 (1993).
- Kresse, G. & Furthmüller, J. Efficiency of ab-initio total energy calculations for metals and semiconductors using a plane-wave basis set. *Comput. Mater. Sci.* **6**, 15–50 (1996).
- Perdew, J. P., Burke, K. & Ernzerhof, M. Generalized gradient approximation made simple. *Phys. Rev. Lett.* **77**, 3865–3868 (1996).
- Dudarev, S. L., Botton, G. A., Savrasov, S. Y., Humphreys, C. J. & Sutton, A. P. Electron-energy-loss spectra and the structural stability of nickel oxide: an LSDA+U study. *Phys. Rev. B.* **57**, 1505–1509 (1998).

Acknowledgements

Q.W. thanks Renault S.A.S for PhD funding. J.-M.T. acknowledges the funding from European Research Council (ERC) (FP/2014)/ERC grant/project no.

670116-ARPEMA. A.M.A. and A.V.M. are grateful to Russian Science Foundation for the financial support (grant no. 20-43-01012). Access to the TEM facilities has been granted by Advance Imaging Core Facility of Skoltech. We thank the ROCK beamline at SOLEIL (Gif-sur-Yvette, France) for X-ray spectroscopy experiments (financed by the French National Research Agency (ANR) as a part of the 'Investissements d'Avenir' programme, reference ANR-10-EQPX-45; proposal nos. 20171234 and 20190596). HAXPES measurements were performed at GALAXIES beamline at the SOLEIL Synchrotron, France under proposal nos. 20171035 and 20190646. This work used resources of the Advanced Photon Source (11-BM), a US Department of Energy (DOE) Office of Science User Facility operated for the DOE Office of Science by Argonne National Laboratory under contract no. DE-AC02-06CH11357. NPD measurements were performed using the ECHIDNA instrument at ANSTO (Sydney, Australia). We are grateful to A. Iadecola for the help during XAS measurements. We thank S. Trabesinger, D. Giaume, M.F. Lagadec, W. Yin, A. Perez, B. Li, G. Yan, G. Assat and J. Vergnet for fruitful discussions. We acknowledge the staff of the MPBT (physical properties, low temperature) platform of Sorbonne Université for their support.

Author contributions

Q.W., S.M. and J.-M.T. conceived the idea and designed the experiments. M.D. and B.P. performed NMR measurements. J.C./Y.-S.Y., R.D. and J.W./W.Y. performed and interpreted the XANES/extended X-ray absorption fine structure, HXAPES and mRIXS measurements. M.A. collected the NPD data, G.R. analysed and interpreted the SXRD and NPD patterns and performed the magnetic measurements while A.V.M. and A.M.A. collected and interpreted all the microscopy data. Last, L.Z. performed the OEMS measurements and M.C. supervised the project. M.-L.D. performed the theoretical calculations and contributed to the overall interpretation of the results. J.-M.T., A.M.A., S.M. and Q.W. wrote the paper, with contributions from all authors.

Competing interests

The O₃-Na(Li_{1/3}Mn_{2/3})O₂ material is patented by Renault (inventors Q.W., M.C., S.M. and J.-M.T.) with patent application number B19-5233FR (pending).

Additional information

Supplementary information is available for this paper at <https://doi.org/10.1038/s41563-020-00870-8>.

Correspondence and requests for materials should be addressed to J.-M.T.

Peer review information *Nature Materials* thanks Naoaki Yabuuchi and the other, anonymous, reviewer(s) for their contribution to the peer review of this work.

Reprints and permissions information is available at www.nature.com/reprints.